Nondestructive assay system of radioactive waste steel box based on tomographic gamma scanning emission measurement*

Xi Huang,[1] Kaiming Yuan,[2] Hua Chen,[1] Jinhui Qu,[3] Yonggang Yuan,[1, †] and Zhaoyi Tan[1, ‡]

[1]*Institute of Nuclear Physics and Chemistry, China Academy of Engineering Physics, Mianyang Sichuan 621000, China*
[2]*Northwestern Polytechnical University, Xian Shanxi 710129, China*
[3]*East China University Of Technology, Nanchang JiangXi 330014, China*

Nondestructive assay (NDA) plays a pivotal role in radioactive waste management. It can accurately evaluate the activity distribution of target nuclide without destroying the original form of the waste, which can provide the crucial basis for subsequent safe classification, proper storage, and scientific disposal. In this paper, a nondestructive assay prototype of radioactive waste steel box is introduced. Given the large size and thickness of the steel box, the emission measurement method in tomographic gamma scanning (TGS) was employed. The Monte Carlo method was utilized to achieve the passive efficiency calibration of the detection system. In the designed prototype, three high-purity germanium (HPGe) detectors mounted on the measurement support platform were used to efficiently measure the full-energy peak counting rate of target nuclides. Based on the Boosted-Gold algorithm, the reconstruction of the radioactive waste activity distribution in steel box was accomplished. The errors of the actual activity measurement are less than 50% and 80% in uniform medium (air, water and sand) and nonuniform medium (aluminum components), respectively. Moreover, the reconstructed activity distribution shows a high degree of consistency with the actual activity distribution. These results validate the capability of the proposed prototype and fully meet the requirements of nondestructive assay of radioactive waste steel box.

Keywords: Nondestructive assay, tomographic gamma scanning, radioactive waste steel box

I. INTRODUCTION

Nuclear energy has served as a clean substitute for fossil fuels, meeting approximately 11% to 20% percent of the global energy demands[1, 2]. However, in the course of nuclear energy development, not only the numerous decommissioned nuclear facilities generate copious amounts of radioactive waste, but also the production, processing, storage, transportation, and utilization of nuclear materials[3, 4]. The improper handling of radioactive waste constitutes a critical environmental health concern.[5]. Prior to final disposal of radioactive waste, precise identification of contained nuclides and quantitative measurement of their activity distribution constitute critical safety prerequisites. While conventional destructive chemical analysis methods rely on representative sampling followed by laboratory examination[6–8], current nondestructive assay primarily employ two gamma-ray spectroscopic approaches: Segmented Gamma Scanning (SGS) and Tomographic Gamma Scanning (TGS).

SGS is mainly used for the quantitative measurement of radionuclides and their content in unevenly distributed medium and low density media[9, 10]. It scans the sample by axial segmentation and radial uniform rotation, and obtains the linear attenuation coefficient of each segmented sample medium by transmission measurement[11, 12]. Then, the γ attenuation of the measured sample is corrected by the linear attenuation coefficient. The accuracy of the measurement results of SGS depends on the attenuation constant of the radioactive medium, the volume of the radioactive sample and the location of the detectors. In order to reduce the measurement error of SGS system and improve the accuracy of detection, some improvement methods based on traditional SGS have been proposed[13, 14]. However, SGS is still not suitable for radioactive samples in non-drum packaging and high-density media cases.

In order to overcome the limitations of SGS, the prototype with TGS was successfully developed [15–17]. TGS is an improvement and a development of SGS, TGS scans the target object from two-dimensional to three-dimensional, not only the axial segmentation scanning, but also the translation and rotation scanning after segmentation for each layer[18–20]. In TGS, the distribution of linear attenuation coefficient are obtained by transmission measurements. Then the actual distribution of the nuclides activity in the sample can be obtained by using the linear attenuation coefficient to correct the activity distribution measured by emission measurement. Combining TGS with virtual point detector method, the accuracy of measurement results of TGS is verified. The results show that the actual measurement results of the activity distribution are in good agreement with those of TGS [21, 22]. Based on the simulation detection system of radioactive waste drum, some models for estimating voxel effect in TGS imaging technology is presented, which confirms the possibility of measuring non-uniform medium waste drum by TGS technology[23–25].

At present, the research of nondestructive assay of radioactive distribution in nuclear waste drums is mainly focused on the improvement of TGS technology[26–29]. Based on the conventional transmission equation and equivalent gamma-ray track length modified by Monte Carlo method, a novel reconstruction algorithm of transmission image for tomographic gamma scanning is proposed. And this algorithm is implemented by simulation[30]. The Neighborhood Homogeneous Measurement(NHM) is proposed to process the salt-

* Supported by the Nuclear Facilities Decommissioning and Radioactive Waste Management Project, State Administration of Science, Technology and Industry for National Defense (No. 2019-1273)
† Corresponding author, yyg_2000@yeah.net
‡ Corresponding author, liu315351@163.com

pepper noise of TGS image system, which avoids the shortcomings of traditional median filtering algorithm[31]. A new algorithm, based on total variation minimization, is presented to reconstruct the voxel transmission images in greater detail with the same number of measurements, and precisely describes the attenuation process. The small voxel size decreases the effect of the inhomogeneity and makes the result more accurate[32]. Furthermore, In order to save time, small number of data is measured by dividing the drum into several large voxels, which leads to the inaccurate TGS images. Therefore, an improved algebraic reconstruction technique (IART) is proposed to reconstruct TGS images. The total variation minimization method and the self-adaptive relaxation factor are applied to improve the iterative process of traditional algebraic reconstruction technique (ART)[33]. In addition, an improved NMO-OSEM (Non-minimization optimization OS-EM) method is designed, which is an iterative algorithm with corrected initial values optimized by non-minimization optimization method[34].

Traditional reconstruction algorithms need the same amount of projection data as the pixel value of the transmission image, which requires a long time to scan and severely limits the industrial application of TGS. In recent years, there are methods that combine reconstruction algorithm with artificial intelligence to optimize TGS measurement process and accuracy. Sparse angle scanning is an optimal approach to improve the efficiency of the TGS system, but the amount of data generated by sparse angle scanning is difficult to support traditional algorithms, which leads to the blurs and artifacts in the reconstructed image. The algebraic reconstruction technique (ART) combined with the Residual Network(ResNet) was designed to reconstruct TGS transmission images. [35]. Moreover, when measuring a waste drum with uniformly distributed medium, the counting rates of three detectors at different positions can be input into a trained neural network, which can directly output the equivalent annular source, ultimately achieving accurate reconstruction of the total activity of radionuclides inside the waste drum [36].

However, for the actual nondestructive measurement of radioactive waste packaged in steel boxes, the size and thickness of steel box are much larger than that of steel drums, it is difficult to achieve transmission measurement in TGS, and only one case was reported. In which, the radioactivity of the steel box was assumed to be a special "image", the steel box was divided into $2\times5\times3$ voxels, based on the simulated efficiency matrix and the characteristic γ ray counting rates measured by the experiment, the reconstruction process was carried out[37]. However, in this work, the division of the voxels is rough and the experimental verification method is quite simple, which results in that the performance and reliability of the method cannot be well explained.

Therefore, in this paper, a nondestructive assay system prototype of radioactive waste steel box will be introduced. Considering the large size and thickness of the steel box, the emission measurement method in tomographic gamma scanning (TGS) will be utilized. Monte Carlo method is used to realize the passive efficiency calibration of the detection system. In the prototype, three high-purity germanium (HPGe) detectors installed on the automatic carrier platform are designed to efficiently measure the full-energy peak counting rate of target nuclides. Based on the Boosted-Gold algorithm, the reconstruction of the radioactive waste activity distribution in steel box will be completed. The actual activity measurement tests, based on both uniform and nonuniform mediums, are carried out to verify the capability of the proposed prototype.

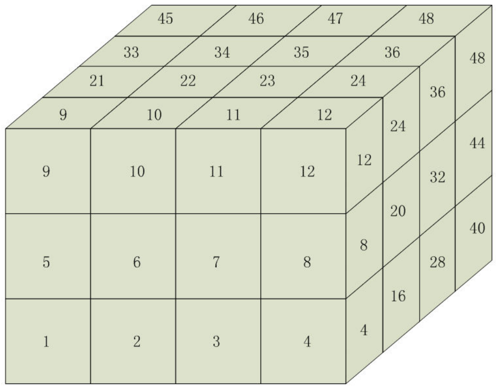

Fig. 1. The divided steel box model

II. METHOD

To begin with, as illustrated in Fig. 1, the model of target steel box, which has actual dimensions of 1573 mm$\times$1565 mm$\times$1331 mm, is divided into three equal layers. Each layer is further subdivided into 16 voxels, resulting in a total box model composed of 48 voxels. The voxel labeling follows a sequential three-dimensional ordering convention, left-to-right in the horizontal plane, inferior-to-superior in the vertical dimension, and anterior-to-posterior in the depth direction, as graphically represented in Fig. 1. The designed non-destructive assay system can obtain the activity of the target nuclide in each voxel, by nondestructive measurement around the steel box, under both the point source and volume source cases.

The system diagram is shown in Fig. 2. For the mainly considered high-energy gamma nuclides (^{60}Co, ^{152}Eu) in radioactive waste, three HPGe detectors are used to measure the gamma spectra, simultaneously. The detector group comprises three detectors that are vertically arranged. The activity reconstruction process is carried out based on leveraging the full-energy peak counting rate that is induced by the highest-energy gamma photon emitted from the radioactive waste. By partitioning the steel box depicted in Fig. 1, each side of the steel box is subsequently divided into 3 layers and 12 two-dimensional regions. The center point of each two-dimensional region is designed as a spectrum measurement point.

The detector array, incorporating a lead collimator with three square apertures, enables precise three-layer radiation measurements. To minimize voxel interference during collimator design, critical parameters including aperture geome-

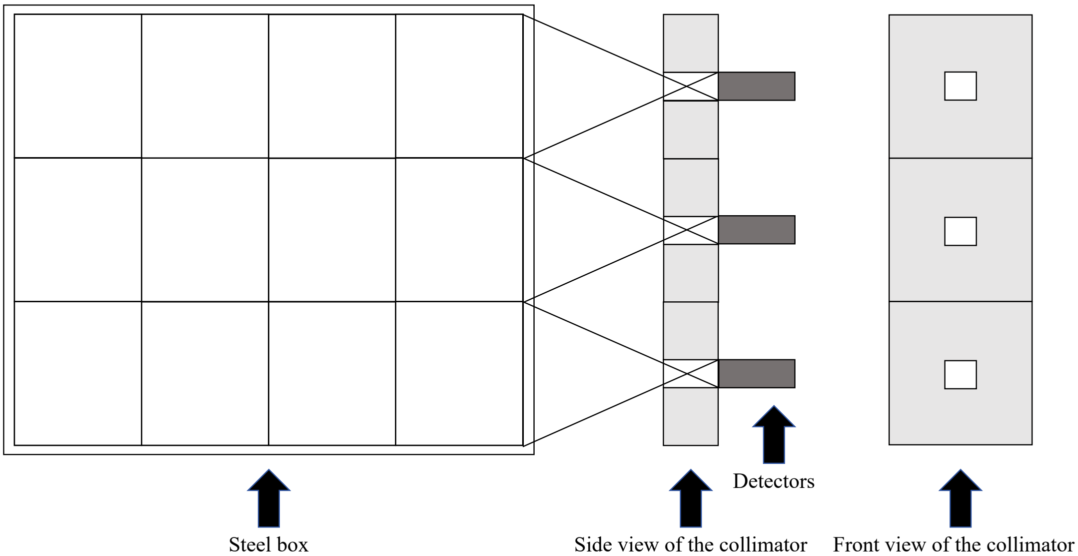

Fig. 2. Measurement system

try, collimation depth, and shielding thickness must be optimized following distance determination. This optimization ensures spatial alignment between each detector's field-of-view and its corresponding two-dimensional region on the side of steel box, while effectively suppressing background noise and cross-talk from adjacent voxels. By conducting four measurements at designated positions, the system achieves efficient full-coverage measurements for a single side. As depicted in Fig. 3, a total of 16 measurement points are arranged, with each sampling location visually indicated by gray dots.

The measurement procedure involves sequential scanning of the steel box through rotational positioning. Upon completing measurements on one side, the detector array retracts to allow a 90 degrees rotation of the steel box, after which scanning proceeds to the adjacent side. The whole procedure requires 16 measurement with three intermediate rotations, ultimately achieving comprehensive coverage of all four sides. Twelve energy spectra of each side are spatially organized in left-to-right and bottom-to-top configuration, with the four surfaces numbered counterclockwise from the initial scanning face. Notably, the sequential arrangement of these 48 measurement points (distributed across 48 two-dimensional regions in 4 sides) differs from the three-dimensional voxel arrangement of the steel box. Figure 3 illustrates the vertical measurement positions with gray dots, where the leftmost nuber corresponds to the lowest detection point and the rightmost to the uppermost one. Subsequent analysis focuses on quantifying the full-energy peak counting rate contributions from these 48 measured spectra to the steel box's radioactive activity distribution.

For the TGS, the transmission measurement is performed in advance. The gamma-ray emitted by the transmission source passing through a material follows the to Beer's law,

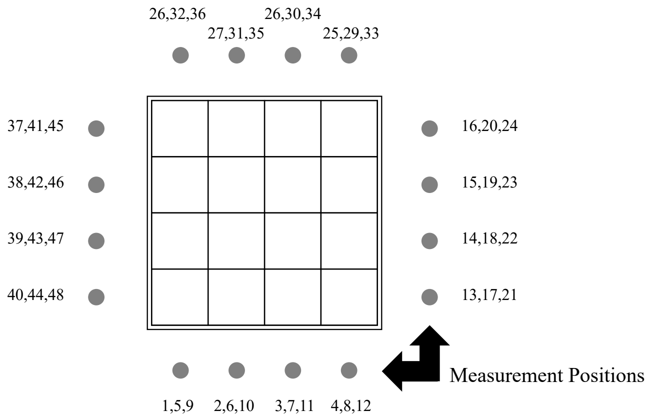

Fig. 3. Measurement positions diagram

which satisfies

$$N_k = N_0 e^{\sum_{i=1}^{I} -\mu_i x_{ki}}, \tag{1}$$

where N_k indicates the full-energy peak counting rate in the k-th transmission measurement and N_0 indicates the full-energy peak counting rate of a certain energy, which is attenuated by air only, μ_i is the linear attenuation coefficient of the i-th voxel, $j \in [1, 48]$, x_{ki} is the transmitting track length of the gamma-ray passing through the i-th voxel when the detector array at the k-th transmission measurement. Each voxel is supposed to be uniform both in transmission and emission measurement. Let $c_k = -\ln(N_k/N_0)$, from (1) one can have

$$\sum_{i=1}^{I} -\mu_i x_{ki} = c_k, \tag{2}$$

where c_k and x_{ki} can be measured and calculated, respec-

tively. By a statistical iterative method, the linear attenuation coefficient matrix can be obtained. Then the gamma-ray emitted by the radioactive waste in the steel box passing through the medium is considered in the emission measurement.

$$N_k = \alpha \sum_{n=1}^{N} A_n E_n e^{\sum_{i=1}^{I} -\mu_i x_{ki}^n}, \tag{3}$$

where N_k indicates the full-energy peak counting rate in the k-th emission measurement. α is the branching ratio of the gamma ray, A_n is the activity of the concerned nuclide in the n-th voxel, E_n is the detection efficiency when a gamma photon with certain energy is emitted from the n-th voxel without attenuation. μ_i is the linear attenuation coefficient of the i-th voxel which is obtained from the transmission measurement. x_{ki}^n is the transmitting track length of the gamma-ray emitted in the n-th voxels passing through the i-th voxel when the k-th measurement is performed. Under the uniform medium conditions, one can have

$$N_k = \alpha \sum_{n=1}^{N} A_n E_n e^{\mu x_k^n}, \tag{4}$$

let $R_{kn} = \alpha E_n e^{\mu x_k^n}$, (4) can be converted into

$$N_k = \sum_{n=1}^{N} R_{kn} A_n, \tag{5}$$

and its matrix form can be obtained as

$$\mathbf{N} = \mathbf{R} \cdot \mathbf{A}, \tag{6}$$

where $\mathbf{N}$ is the full-energy peak counting rate vector, $\mathbf{R}$ is the system response function matrix, and $\mathbf{A}$ is the activity vector of the 48 voxels.

The matrix $\mathbf{R}$ contains the detection efficiency parameters and the linear attenuation coefficient, which can be obtained by passive calibration method and transmission measurement, respectively. However, due to the large size of the steel box, the calibration source and transmission source with high activity are needed, which brings great challenges to radiation safety and protection. Therefore, the passive calibration method is adopted. The system response function matrix $\mathbf{R}$ is obtained by the Monte-Carlo software. The response function matrix libraries for volume sources and point sources have been computed separately. Each library contains multiple response function matrices corresponding to material densities ranging from that of air (0.001 g/cm^3) to aluminum (2.7 g/cm^3), with a density increment of 0.3 g/cm^3 between successive response function matrices. Figure 4 shows a response function matrix example of a point source in air. Fig. 4(a) plots the entire response function matrix as a bar chart. Each column in Fig. 4(a), corresponding to a voxel number, shows the expected contribution of gamma rays emitted from that voxel to the full-energy peak counting rates in the 48 measured energy spectra. And the full-energy peak counting rates are obtained from the characteristic energy gamma-rays (^{60}Co:1332 keV, ^{152}Eu: 1408 keV) which are emitted during the decay of an nuclide atom.

As can be seen from Fig. 4(b), when a gamma photon is emitted from the first voxel, the full-energy peak counting rate of the first measurement point and the 40-th measurement point both exhibit the maximum values, since these two measurement points are equal and the closest to the emitting voxel. The full-energy peak counting rate of the energy spectrum of the 13-th and 28-th measuring points both are the local maximum values, since these two measurement points, who can cause the response of the detector under the presence of the lead collimator, have the local minimum distance from the emitting voxel. The local minimum distance is the width of three voxels. Figure 4(d) shows a similar situation, in which the gamma photon is emitted from the 48-th voxel. In Fig. 4(c), gamma photons are emitted from the 24-th voxel. The full-energy peak counting rates of the energy spectra decreases from the nearest 22-th measuring point and the 12-th, 33-th,47-th measuring point, which have 0,1,2 and 3 voxels away from the emitting voxel, respectively.

With the response function matrix, the Boosted-Gold algorithm is adopted to perform the activity reconstruction by obtaining the least squares solution of (6)[38], which can be defined as

$$\mathbf{A}^{k+1} = \mathbf{A}^k + \delta^k(\mathbf{R}^T\mathbf{N} - \mathbf{R}^T\mathbf{R}\mathbf{A}^k), \tag{7}$$

where δ^k is a introduced relaxation coefficient vector, whose element δ_i^k is defined as

$$\delta_i^k = \frac{A^k}{\sum_{l=1}^{N}(\mathbf{R}^T\mathbf{R})_{il}A_l^k}, \tag{8}$$

where $(\mathbf{R}^T\mathbf{R})_{il}$ indicates the element in the i-th row, j-th column of the matrix $\mathbf{R}^T\mathbf{R}$, N is the number of response functions that constitute the response matrix. With (7) and (8), the iterative formula can be derived as

$$A_i^{k+1} = \frac{(\mathbf{R}^T\mathbf{N})A_i^k}{\sum_{l=1}^{n}(\mathbf{R}^T\mathbf{R})_{il}A_l^k}. \tag{9}$$

After a given number of iterations, shown in (9), a nonlinear enhancement process is performed, which is given as follows.

$$A_i^0 = (A_i^k)^p, \tag{10}$$

where $p > 1$ is the power exponential enhancement coefficient. And take the enhancement result as the initial value of (9). After a given number of enhancement, the solution that satisfies the convergence condition or the iteration and enhancement number conditions is obtained. The convergence condition is shown below

$$\frac{||\mathbf{A}^{k+1} - \mathbf{A}^k||}{||\mathbf{A}^k||} < \varphi, \tag{11}$$

where, A^k is the result of the k-th iteration, and A^{k+1} is the

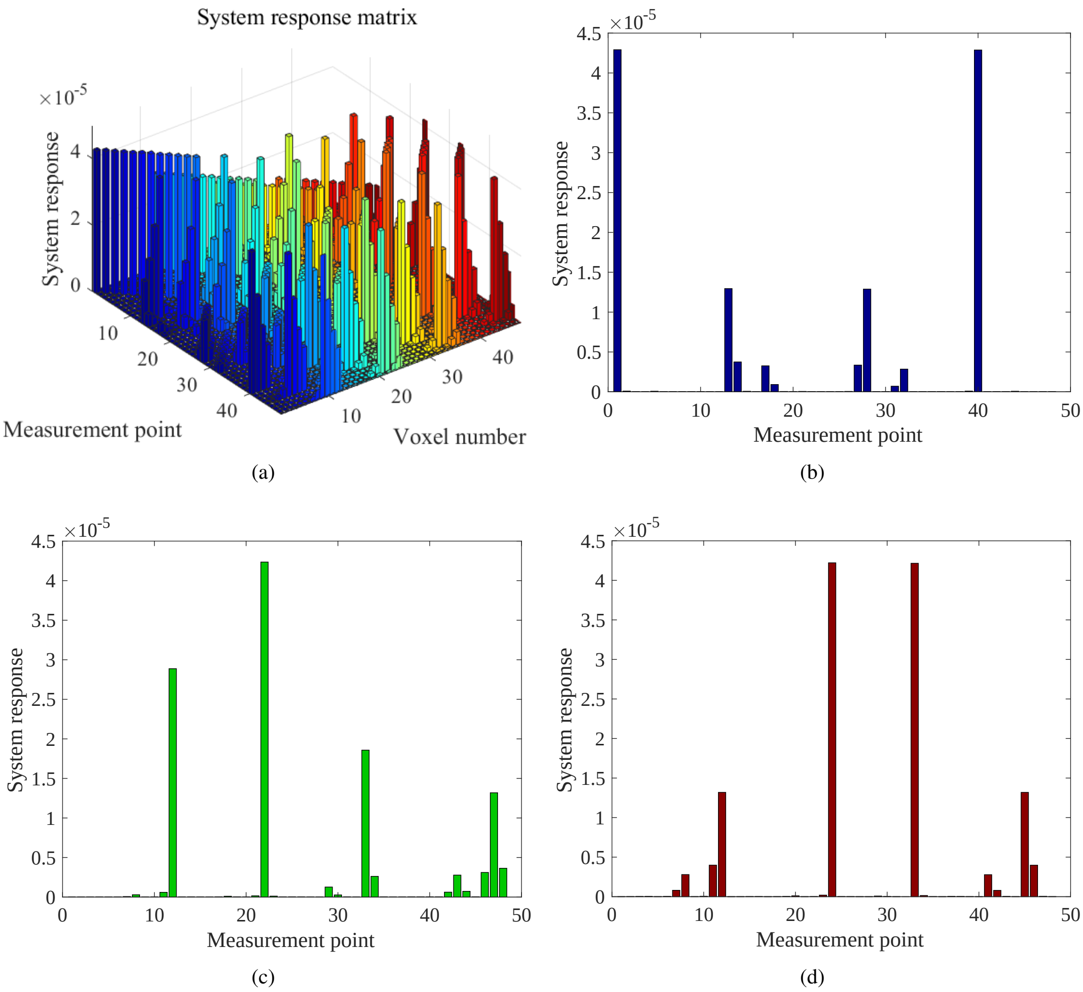

Fig. 4. An example of system response function matrix. (a) is the histogram of the system response function matrix(48×48). (b), (c) and (d) are the full-energy peak counting rates vectors histogram of the radioactive source placed in the first, 24-th and 48-th voxels, respectively.

$k+1$-th iteration, φ is the given iteration residual precision. $||\cdot||$ indicates the Euclidean norm.

The algorithm iteration process can be systematically described through four sequential stages. In the initialization phase, critical parameters including the initial matrix $\mathbf{A}^k$, iteration threshold k, enhancement threshold K, and termination criterion φ are established. The process then executes two key operations: (1) applying the recursive formula (9) for matrix updating, and (2) evaluating the convergence condition (11). When the enhancement condition is triggered, the algorithm implements a enhancement mechanism by adjusting the factor p to accelerate convergence. This process continues until the termination criterion or iteration threshold are satisfied, ultimately yielding reconstructed activity distributions and total activity of radioactive waste within the steel box.

III. EXPERIMENT

In the nondestructive assay of radioactive waste activity within steel box packaging, the gamma nuclides with high energy and long half-life are mainly concerned. Therefore, the response function matrices of the highest energy gamma photon of ^{60}Co and ^{152}Eu are calculated in this paper, under both point source and volume source cases. Based on the response function matrices, simulation experiments, actual experiments in uniform medium and non-uniform medium were carried out, respectively. In these experiments, the maximum energy full-energy peak counting rates of 48 measurement points were obtained through the Monte-Carlo simulation or actual measurement. Based on the designed method in Section II, the reconstructed total activity and activity distribution of the steel box are given, and the relative errors are evaluated.

TABLE 1. Activity reconstruction results of simulation data

Activity distribution	Total activity of simulation	Total activity of reconstruction	Relative error
Pulse	1.00e+09	0.99e+09	0.6%
Linear	1.18e+12	1.18e+12	0.12%
Random	2.90e+12	2.79e+12	3.8%

A. Simulation Experiment

In order to verify the effectiveness and robustness of designed method, a simulation experiment was presented. For the 48 voxels in the steel box model, the pulse, linear and random distribution of radioactive waste cases were simulated (^{60}Co@1332 keV). The full-energy peak counting rates of 48 measurement points with different distribution were simulated by the Monte-Carlo software. Gaussian white noise was added to the simulated vector, to characterize the influence caused by the error of Monte-Carlo model and calculation algorithm of the full-energy peak counting rate for the actual measured spectrum. The noise data was brought into the algorithm, and the reconstructed results were calculated and compared with the actual simulation data. The reconstructed activity distribution of the three cases is shown in the Fig. 5. The simulation total activities, reconstructed total activities and relative errors are shown in Table. 1. In the pulse distribution, illustrated in Fig. 5(a), the activity of the 21-th voxel was set as 1.00e+09 Bq, its reconstruction results, including the relative error of the simulated and reconstructed total activities and the reconstructed distribution, show a good conformance. In the linear distribution, illustrated in Fig. 5(b), the activities of the first to the 48-th voxel was set to be linear from 1.00e+09 Bq to 4.80e+10 Bq, its reconstructed activity distribution result shows a linear distribution with certain fluctuations, and the reconstructed total activities shows a less relative error. In the random distribution, illustrated in Fig. 5(c), the activities of the second, 9-th, 21-th, 27-th, 28-th and 32-th voxels were set to be 3.00e+09 Bq, 5.00e+09 Bq, 1.00e+09 Bq, 4.00e+09 Bq, 6.00e+10 Bq, 8.00e+10 Bq, 1.00e+10 Bq, respectively.

B. Actual Experiment Under Uniform Medium

The self-developed actual nondestructive assay system is shown in Fig. 6, it mainly consists of three parts: a radioactive waste steel box, a mechanical control platform and a detection module. The steel box, marked with (1) in Fig. 6, which is a FA-IV steel box with a size of 1573 mm×1565 mm×1331 mm.

The mechanical control platform, marked with (3) in Fig. 6, consist of a steel box support platform and a measurement support platform. The size of steel box support platform is 1600 mm×1600 mm×830 mm, which is mainly used for 360° rotation and weighing of the steel box. Four weighing meters are respectively installed at the four corners of the support platform. An industrial computer is utilized to collect the actual weight of the steel box. By subtracting the weight of the steel box from the collected data, the density information of the radioactive waste can be obtained. The steel box can be transported to the steel box support platform by a forklift. The steel box support platform is equipped with four protruding snap devices, which ensure the stability of the box during rotation. The support platform rotates at a speed of 2 degrees per second and has a maximum weighing capacity of 10 tons. The measurement support platform has three degrees of freedom, X, Y, and Z axes. It is constructed by integrating three individual platforms corresponding to the X, Y, and Z axes. The overall dimensions of this platform are 2190 mm×3660 mm×2280 mm.

The detection module, marked with (2) in Fig. 6, is precisely positioned at the Z platform. This module is further composed of a detector array, which is responsible for measuring gamma spectra, and a shield module, designed in Section II to protect against the external interferences from other voxels. Moreover, the distance between the steel box and the front end of the detectors is taken as 40.6cm, and the side length of the collimator hole in front of the detectors is taken as 8.3cm, to make sure that the detector axially cover one side of a voxel.

Based on the aforementioned measurement system, the experimental validation utilized three uniform media (air, water, and sand) to assess system performance. A ^{60}Co (2.22e+07 Bq) source and a ^{152}Eu (5.17e+07 Bq) source were used for activity reconstruction tests. In the sand media case, two additional sources with different activities (a ^{60}Co (4.32e+07 Bq) and a ^{152}Eu (1.02e+08 Bq)) were used to further verify the effectiveness of the designed system. Besides, to rigorously evaluate system robustness, three distinct source configurations were implemented in the steel box: (1) solitary ^{60}Co placement, (2) solitary ^{152}Eu placement, and (3) simultaneous dual-source deployment.

Figure 7 gives the experimental site and reconstructed activity distribution under different sources and media. Figs. 7(a), 7(e) and 7(i) show the experimental sites under air medium, water medium and sand medium, respectively. In the air and water medium, the radioactive source was placed in the center of the voxel by hanging on the top of the steel box. In the sand medium, the radioactive source was inserted into the sand by an aluminum rod. Figures 7(b), 7(c) and 7(d) respectively show the reconstructed activity distributions when single ^{60}Co source, single ^{152}Eu source and both sources were placed in the steel box under air medium. Red indicates the activity of ^{60}Co source, blue indicates the activity of ^{152}Eu source, and the color depth of the voxel in the steel box is proportional to the activity in the voxel. Figures 7(f)-7(h) and 7(j)-7(n) were drawn with the same principle. The actual voxel placement of radioactive sources in each case can be seen in Table 2. It is worth mentioning that, in order to verify the reliability of the designed method, two additional tests were carried out by changing the activity of the radioactive source in Figs. 7(m) and 7(n), in which the activity of the ^{60}Co and ^{152}Eu were changed to 1.02e+08 Bq and 4.32e+07 Bq, respectively. Table 2 shows the measured density of each medium, the location of the radioactive sources

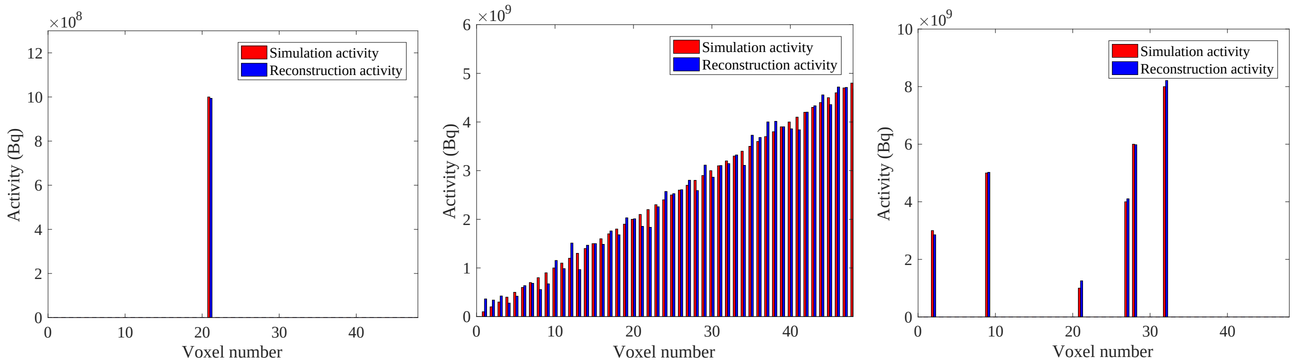

(a) (b) (c)

Fig. 5. Activity reconstruction results of radioactive sources under three conditions. (a), (b) and (c) correspond to the pulse, linear and random conditions, respectively.

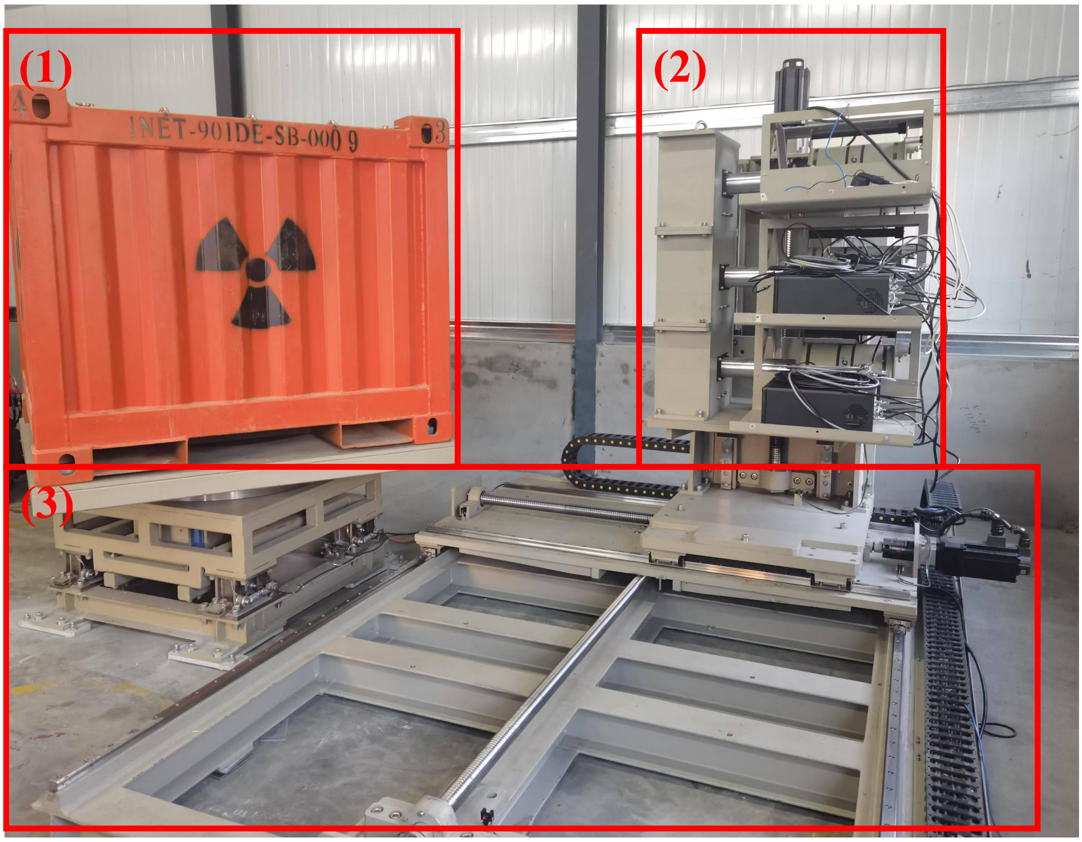

Fig. 6. Nondestructive assay system prototype of radioactive waste steel box. (1) is the steel box to be measured, (2) is the detector array, (3) is the mechanical control platform.

in certain medium, the reconstructed activity, the standard activity and the relative errors. In the three media, the first two rows are single-source placement cases, and the remaining row is the dual-source placement case. As can be seen from Table 2, the relative error ranges of air, water and fine sand are -27.3%-26.6%, -37.5%-48.5% and -45.6%-32% respectively. The maximum values of the reconstructed nuclide activity distribution are consistent with the actual voxel placed in the radioactive source, and there are significant differences between them and other voxels.

C. Actual Experiment Under Nonuniform Medium

The first two subsections demonstrated the successful reconstruction of radioactive waste activity in steel box using

TABLE 2. Activity reconstruction results for uniform medium.

Medium	Density	Voxel number		Measured Activity (Bq)		Standard Activity (Bq)		Relative error	
		^{152}Eu	^{60}Co	^{152}Eu	^{60}Co	^{152}Eu	^{60}Co	^{152}Eu	^{60}Co
Air	0.001	-	32	-	2.81e+07	-	2.22e+07	-	26.6%
		31	-	4.14e+07	-	5.17e+07	-	-19.9%	-
		23	34	3.76e+07	2.69e+07	5.17e+07	2.22e+07	-27.3%	21.2%
Water	0.8215	-	2	-	1.29e+07	-	2.22e+07	-	-41.9%
		2	-	3.23e+07	-	5.17e+07	-	-37.5%	-
		2	15	3.36e+07	1.65e+07	5.17e+07	2.22e+07	-35.1%	-25.6%
Sand	1.2881	-	30	-	2.70e+07	-	2.22e+07	-	21.6%
		11	-	4.30e+07	-	5.17e+07	-	-16.8%	-
		23	34	5.17e+07	2.88e+07	5.17e+07	2.22e+07	-27.3%	21.2%
		30	11	2.81e+07	2.93e+07	5.17e+07	2.22e+07	-45.6%	32%
		19	30	7.81e+07	3.33e+07	1.02e+08	4.32e+07	-23.4%	-22.9%

simulated and measured data under uniform medium condition. However, in practical applications of the steel box, achieving a perfectly uniform medium remains impractical even with meticulous arrangement. To address this realistic challenge, this section employs irregularly shaped aluminum components to simulate nonuniform measurement medium within the steel box. This experimental design enables comprehensive evaluation of the proposed algorithm's stability and robustness in nonuniform environments.

Figure 8 shows the experimental site and reconstructed activity distribution under aluminium medium, in which, the radioactive source was inserted into the aluminum by mounting an aluminum rod. Figs. 8(b), 8(c) and 8(d) respectively demonstrate the reconstructed activity distributions when single ^{60}Co source, single ^{152}Eu source and both sources were placed in the steel box, which is same with Fig. 7. Table 3 is in the same format as Table 2. the relative error ranges of aluminium medium are -12.4%-73.9%. The maximum values voxel of the reconstructed activity distribution are consistent with the actual voxel placed in the radioactive source, but there are not significant differences between them and other adjacent voxels, as shown in Fig. 8(d).

With the aforementioned actual experiment under nonuniform and uniform medium, Fig. 9 gives the comparison results between the response functions and the measured full-energy peak counting rates after normalization in four representative cases. Figure 9(a) illustrates the full-energy peak counting rate vector and the corresponding response function for ^{60}Co source in Fig. 7(b). Figures 9(b), 9(c) and 9(d) were obtained with the ^{60}Eu source in Fig. 7(g), ^{60}Eu source in Fig. 7(c) and ^{60}Co source in Fig. 8(d), respectively.

IV. RESULTS AND DISCUSSION

In Section III, the Monte Carlo model was utilized to calculate the full-energy peak counting rate vectors under the given three distributions of radioactive sources. Gaussian noise was superimposed based on the counting rate. The simulation results showed that the error of activity reconstruction results is quite less than 5% after superimposing Gaussian noise, which fully demonstrates the robustness and stability of the reconstruction algorithm. The relative errors observed in analytical outcomes are primarily attributed to two factors: (1) the preconfigured noise levels in the vectors. (2) intrinsic limitations of the analytical algorithm's mathematical approximations.

In the actual experiment under uniform medium, the single and double source tests were carried out under air, water and sand medium. Due to the existence of hanging basket inside the steel box and the error of medium loading and size, the density of water and fine sand medium is smaller than the standard value. Various attempts have been made to locate the radioactive source, including the central and the boundary voxels. The reconstruction results show that the error of the reconstruction results when the radioactive source is placed in the central voxel is generally smaller than that of the boundary voxel. This is mainly because of the existence of the hanging basket and the error of the steel box modeling.

The error range of activity assay results in air medium is -19.9%-28.8%. The error range of activity assay results in water medium is -37.5%- -41.9%. The error range of activity assay results in fine sand medium is -45.6%-32%. The error range of activity assay results in aluminum medium is -12.4%-73.9%, all of which are less than 100%. In uniform medium, the relative error value mainly comes from the geometric position error of radioactive source, the error of analytic algorithm, the error of theoretical calculation response

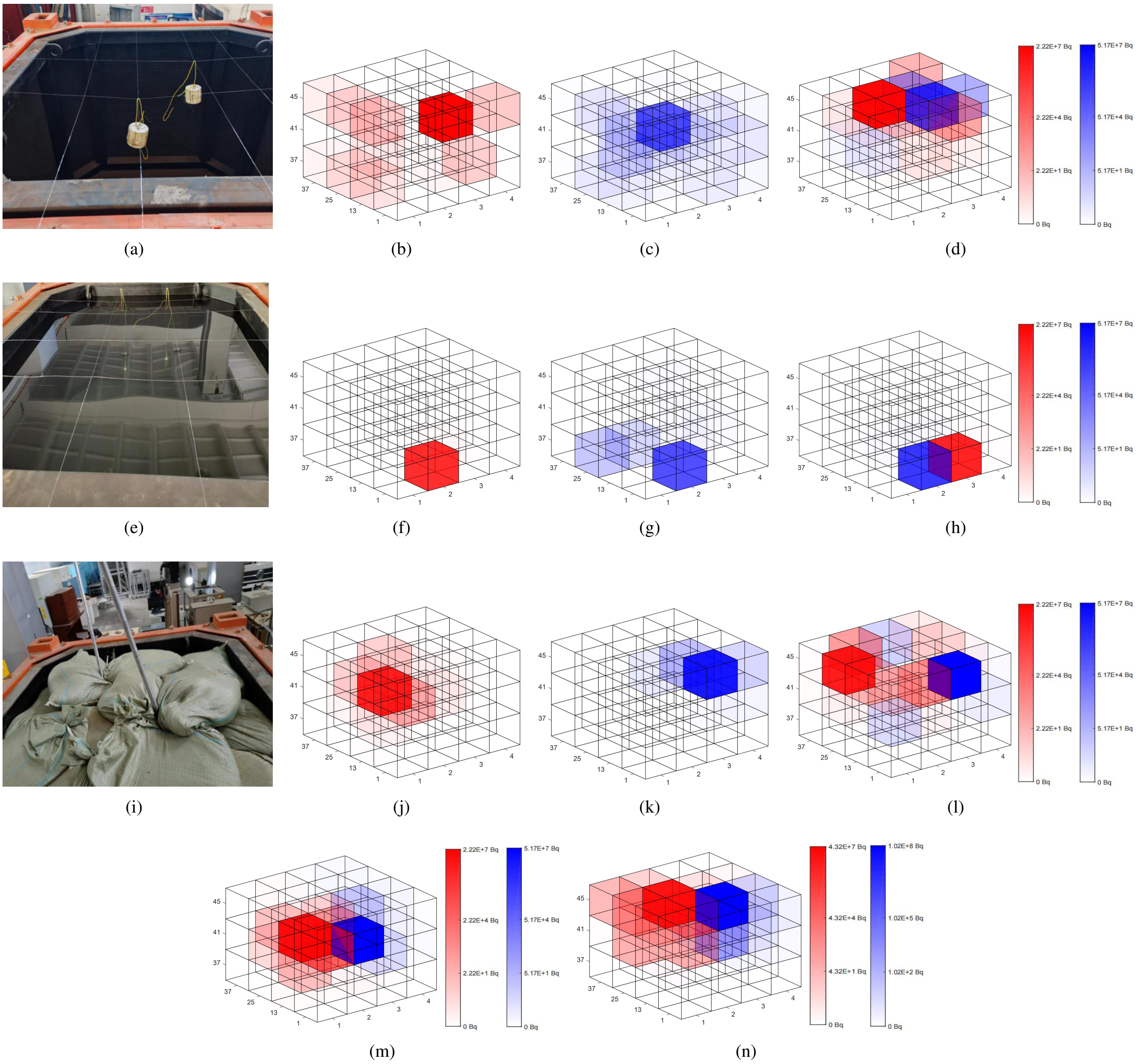

Fig. 7. Experimental sites and reconstructed activity distributions under different sources for uniform medium. (a)-(d), (e)-(h) and (i)-(n) correspond to air, water and sand medium, respectively.

function and actual measurement result, and the error of energy spectrum characteristic peak area calculation.

In the air medium, reconstruction noise is more obvious due to two reasons. The first is due to the large radioactive source activity, resulting in a large dead time of the detector(especially in the boundary voxels), which still brings errors to the full-energy peak counting rate, after calibration. The second reason is that in order to facilitate installation and disassembly, a black hanging basket is installed in the steel box, which is not modeled in the Monte Carlo model, and the density gap is relatively small in the water and sand medium, and the impact is not obvious. At the same time, in the air medium, the radioactive source is placed through the iron wire, and it will shake to a certain extent when the support platform moves and the steel box rotates, which also makes the full-energy peak counting rate and the Monte-Carlo calculation result are in line with the trend, but the counting rate ratio of different detection points is greatly different, which is shown in Fig. 9(a).

Form Fig. 9(b), it can be seen that in the water medium, the actual full-energy peak counting rate is most close to the Monte-Carlo simulation results. This is mainly because the Monte-Carlo model of the steel box in the water medium is the closest to the actual model. In the sand medium, due to the

TABLE 3. Activity reconstruction results for nonuniform medium.

Medium	Density	Voxel number		Measured Activity (Bq)		Standard Activity (Bq)		Relative error	
		^{152}Eu	^{60}Co	^{152}Eu	^{60}Co	^{152}Eu	^{60}Co	^{152}Eu	^{60}Co
Aluminium	0.8006	-	7	-	3.86e+07	-	2.22e+07	-	73.9%
		7	-	5.54e+07	-	5.17e+07	-	7.2%	-
		29	7	4.53e+07	3.86e+07	5.17e+07	2.22e+07	-12.4%	73.9%

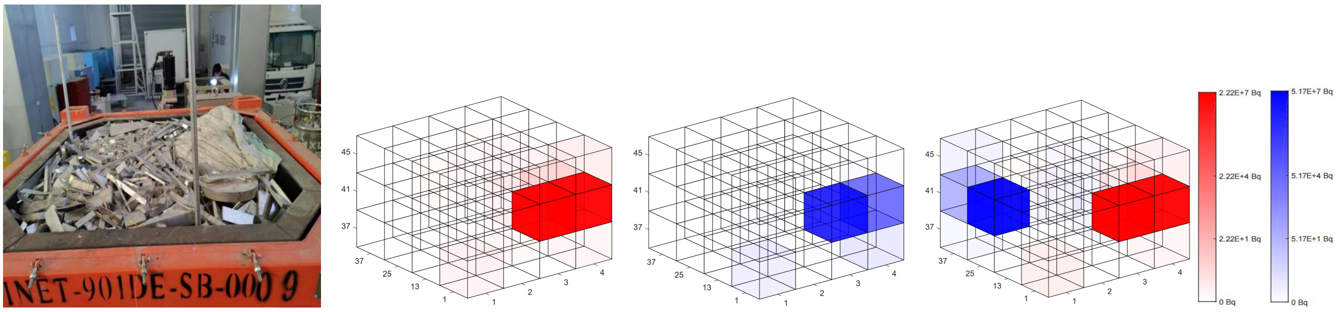

(a) (b) (c) (d)

Fig. 8. Experimental site and reconstructed activity distribution under different sources for nonuniform medium.

use of bagged sand, the gap between the bags and the difference in the water content of the bags, the medium is relatively less uniform, resulting in greater noise in the inversion results. At the same time, the water medium is denser than the air medium, and the radioactive source is placed through the iron wire, which is more stable in the measurement and rotation of the steel box. This also makes the full-energy peak counting rate agree with the Monte-Carlo simulation results in both trend and proportion, which is shown in Fig. 9(b).

In the last medium, we used irregular aluminum components, which can be easily found in radioactive waste, to simulate nonuniform medium. Compared with the waste package solidified with cement, the nonuniformity is greater under this method. From the results of activity reconstruction, the maximum relative error is 73.9%. This has certain performance difference compared with uniform medium. The main reason is that the measured full-energy peak counting rate is too different from the response function. For example, in Fig. 9(d), the counting rate data of 17-th and 18-th measurement points are quite different, resulting in two voxels with similar activity in Fig. 8(d). However, it is worth mentioning that in this extremely heterogeneous medium, the total activity of the algorithm still does not appear more than an order of magnitude error, which also shows the robustness of the system.

In addition, the experimental results of all medium indicate that there is no significant difference between the measurement errors of the single source and those of the dual source in the measurement system. There are two main reasons, first of all, the designed method only utilizes the full-energy peak counting rate of the maximum gamma energy, for the target radionuclide, instead of full-spectrum counting rate. Meanwhile, the prototype is equipped with three HPGe detectors, which have excellent energy resolution. This ensures that the count results of the full-energy peaks of different energies do not interfere with each other. Thus, the simultaneous measurement of the activities of multiple radionuclides is realized.

V. SUMMARY

In this paper, a nondestructive assay system prototype of radioactive waste steel box was introduced, in which the emission measurement method in tomographic gamma scanning (TGS) was adopted. Monte Carlo method was used to realize the passive efficiency calibration of the detection system. In the prototype, three HPGe detectors were used to efficiently measure the full-energy peak counting rate of target nuclides. Based on the Boosted-Gold algorithm, the reconstruction of the radioactive waste activity distribution in steel box was completed. The actual activity measurement error of the system is less than 50% and 80% in uniform medium (air, water and sand) and non-uniform medium (aluminum components), respectively. Moreover, the reconstruction activity distribution shows a high degree of consistency with the actual distribution. These results verify the capability of the proposed prototype and fully meet the requirements of nondestructive assay of radioactive waste steel box.

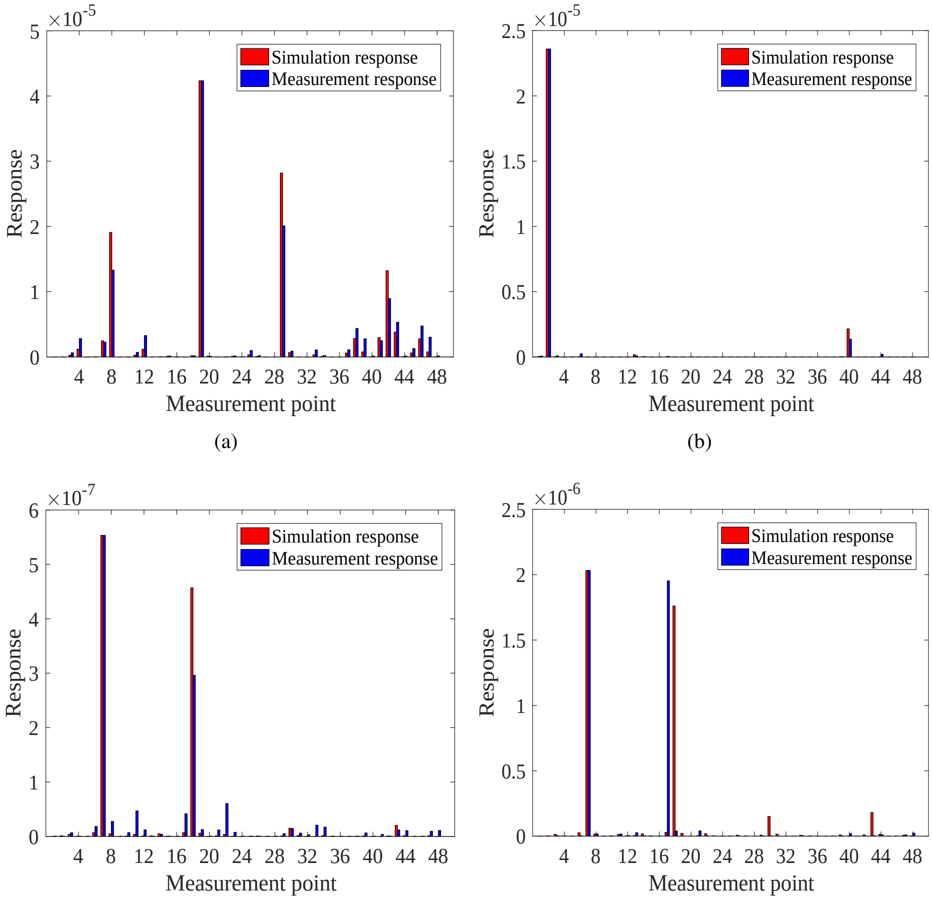

(a) (b) (c) (d)

Fig. 9. Comparison results between the response function and the measured full-energy peak counting rate vectors after normalization

[1] H. S. Kim, Comparison of cost efficiencies of nuclear power and renewable energy generation in mitigating CO_2 emissions. Environ. Sci. Pollut. Res. **28**, 789-795 (2021). doi:10.1007/s11356-020-10537-1

[2] N. K. Katiyar, S. Goel, Recent progress and perspective on batteries made from nuclear waste. Nucl. Sci. Tech. **34**, 33 (2023). doi:10.1007/s41365-023-01189-0

[3] G. A. Wen, J. H. Wu, C. Y. Zou, et al., Preliminary safety analysis for a heavy water-moderated molten salt reactor. Nucl. Sci. Tech. **35**, 106 (2024). doi:10.1007/s41365-024-01476-4

[4] D. Deng, L. Zhang, M. Dong, et al., Radioactive waste: A review. Water Environ. Res. **92**, 1818-1825 (2020). doi:10.1002/wer.1442

[5] S. A. Darda, H. A. Gabbar, V. Damideh, et al., A comprehensive review on radioactive waste cycle from generation to disposal. J. Radioanal. Nucl. Chem. **329**, 15-31 (2021). doi:10.1007/s10967-021-07764-2

[6] Y. W. Chen, J. L. Wang, Removal of cesium from radioactive wastewater using magnetic chitosan beads cross-linked with glutaraldehyde. Nucl. Sci. Tech. **27**, 43 (2016). doi:10.1007/s41365-016-0033-6

[7] M. F. Attallah, S. E. Rizk, S. A. Shady, Separation of $^{152+154}$Eu, ^{90}Sr from radioactive waste effluent using liquid-liquid extraction by polyglycerol phthalate. Nucl. Sci. Tech. **29**, 84 (2018). doi:10.1007/s41365-018-0423-z

[8] A. O. Adeola, K. O. Iwuozor, K. G. Akpomie, et al., Advances in the management of radioactive wastes and radionuclide contamination in environmental compartments: a review. Environ. Geochem. Health. **45**, 2663-2689 (2023). doi: 10.1007/s10653-022-01378-7

[9] J.W. Zhao, W.N. Su, An iterative image reconstruction algorithm for SPECT. Nucl. Sci. Tech. 25, 030302 (2014). doi: 10.13538/j.1001-8042/nst.25.030302

[10] J. K. Sprinkle, S. T. Hsue, Recent advances in segmented gamma scanner assay. Trans. Am. Nucl. Soc. **55** (1987).

[11] E. Laloy, B. Rogiers, A. Bielen, et al., Bayesian inference of 1D activity profiles from segmented gamma scanning of a heterogeneous radioactive waste drum. Appl. Radiat. Isot. **175**, 109803 (2021). doi: 10.1016/j.apradiso.2021.109803

[12] H. Zheng, X. Tuo, W. Zhao, et al., An efficiency function model of segmented gamma scanning for measuring radioactive waste drum. Appl. Radiat. Isot. **199**, 110895 (2023). doi: 10.1016/j.apradiso.2023.110895

[13] S. Patra, C. Agarwal, S.Chaudhury, Full energy peak efficiency calibration for the assay of large volume radioactive waste drums in a segmented gamma scanner. Appl. Radiat. Isot. **144**, 80-86 (2019). doi: 10.1016/j.apradiso.2018.11.014

[14] Y. F. Bai, E. Mauerhofer, D.Z. Wang et al., An improved method for the non-destructive characterization of radioactive waste by gamma scanning. Appl. Radiat. Isot. **67**, 1897-1903 (2009). doi: 10.1016/j.apradiso.2009.05.017

[15] T. Q. Dung, N. D. Thanh, L. A. Tuyen, et al., Evaluation of a gamma technique for the assay of radioactive waste drums using two measurements from opposing directions. Appl. Radiat. Isot. **67**, 164-169 (2009). doi: 10.1016/j.apradiso.2008.08.008

[16] T. Roy, J. Ratheesh, A. Sinha, Three-dimensional SPECT imaging with LaBr3: Ce scintillator for characterization of nuclear waste. Nucl. Instrum. Methods Phys. Res., Sect. A. **735**, 1-6 (2014). doi: 10.1016/j.nima.2013.08.037

[17] T. Roy, M. R. More, J. Ratheesh, et al., Active and passive CT for waste assay using LaBr3 (Ce) detector. Radiat. Phys. Chem. **130**, 29-34 (2017). doi: 10.1016/j.radphyschem.2016.07

[18] T. Q. Dung, A simple gamma technique for the assay of radioactive waste drums. Int. J. Nucl. Energy Sci. Technol. **5**, 290-297 (2010). doi: 10.1504/ijnest.2010.035539

[19] R. J. Estep, T. H. Prettyman, G. A.Sheppard, Tomographic gamma scanning to assay heterogeneous radioactive waste. Nucl. Sci. Eng. **118**, 145-152 (1994). doi: 10.13182/NSE94-A19380

[20] R. Venkataraman, M. Villani, S. Croft, et al., An integrated Tomographic Gamma Scanning system for non-destructive assay of radioactive waste. Nucl. Instrum. Methods Phys. Res., Sect. A. **579**, 375-379 (2007). doi: 10.1016/j.nima.2007.04.125

[21] H. D. Chuong, T. M. Sang, L. G. Thien, et al., Combination of the gamma emission tomography and the virtual point-detector methods for calculating radioactive waste drum by non-destructive assays. Sci. Tech. Develop. J. Nat. Sci. **2**, 214-221 (2018). doi: 10.32508/stdjns.v2i6.884

[22] J. Suran, P. Kovar, J. Smoldasova, et al.. New high-throughput measurement systems for radioactive wastes segregation and free release. Appl. Radiat. Isot. **130**, 252-259 (2017). doi: 10.1016/j.apradiso.2017.09.043

[23] T. Q. Dung. Estimation of systematic error of the gamma tomography for correction of self-attenuation in assay of radioactive waste. **47**, 155 (2013). doi: 10.54607/hcmue.js.0.47.891

[24] D. C. Camp, H. E. Martz, G. P. Roberson, et al., Nondestructive waste-drum assay for transuranic content by gamma-ray active and passive computed tomography. Nucl. Instrum. Methods Phys. Res., Sect. A. **495**, 69-83 (2002). doi: 10.1016/S0168-9002(02)01315-3

[25] S.Tortajada, F. Albiol, L. Caballero, et al., A portable geometry-independent tomographic system for gamma-ray, a next generation of nuclear waste characterization. Sci. Rep. **13**, 12284 (2023). doi: 10.1038/s41598-023-39405-x

[26] Y. Wang, Y. Liu, X. Yao, et al., Design of segmented gamma scanning and tomographic gamma scanning automatic detection system for barreled nuclear waste. J. Radiat. Res. Radiat. Proc. **37**, 61-66 (2019). (**in Chinese**)

[27] H. Yang, X. Y. Zhang, W. G. Gu, et al., A novel method for gamma spectrum analysis of low-level and intermediate-level radioactive waste. Nucl. Sci. Tech. **34**, 87 (2023). doi: 10.1007/s41365-023-01236-w

[28] Y. C. Yan, M. Z. Liu, X. Y. Li, et al., Improved Cohen-Sutherland algorithm for TGS transmission imaging. Nucl. Sci. Tech. **34**, 98 (2023). doi: 10.1007/s41365-023-01238-8

[29] M. Belzunce, C. Verrastro, L. M. Garbino, et al., An attenuated projector for iterative reconstruction algorithm of a high sensitivity tomographic gamma scanner. IEEE Trans. Nucl. Sci. **61**, 975-984 (2014). doi: 10.1109/TNS.2014.2302454

[30] Q. H. Zhang, W. H. Hui, D. Wang, et al., A novel algorithm for transmission image reconstruction of tomographic gamma scaners. Nuc. Sci. Tech. **21**, 177-181 (2010). doi: 10.13538/j.1001-8042/nst.21.177-181

[31] K. X. Peng, X. G. Tuo, B. Cai, et al., An Algorithm of Reduction Salt-Pepper Noise in TGS Images. 2012 International Conference on Computer Science and Electronics Engineering. IEEE, 416-419 (2012). doi: 10.1109/iccsee.2012.15

[32] K. Wang, Z. Li, W. Feng, Reconstruction of finer voxel grid transmission images in tomographic gamma scanning. Nucl. Instrum. Methods Phys. Res., Sect. A. **755**, 28-31 (2014). doi: 10.1016/j.nima.2014.04.046

[33] H. Zheng, X. G. Tuo, S. Peng, et al., An improved algebraic reconstruction technique for reconstructing tomographic gamma scanning image. Nucl. Instrum. Methods Phys. Res., Sect. A. **906**, 77-82 (2018). doi: 10.1016/j.nima.2018.07.095

[34] A. J. He, X. G. Tuo, R. Shi, et al., An improved OSEM iterative reconstruction algorithm for transmission tomographic gamma scanning. Appl. Radiat. Isot. **142**, 51-55 (2018). doi: 10.1016/j.apradiso.2018.09.001

[35] C. M. Wang, R. Shi, X. G. Tuo, et al., Reconstruction of tomographic gamma scanning transmission image from sparse projections based on convolutional neural networks. Nucl. Instrum. Methods Phys. Res., Sect. A. **1039**, 167110 (2022). doi: 10.1016/j.nima.2022.167110

[36] M. X. Shu, C. Y. Shan, W. G. Gu, et al., A neural network-based method for measuring the activity of waste drum. Nucl. Tech. **46**, 120501 (2023). **in Chinese**

[37] Z. J. Guo, P. Nie, Direct measurement method and verification of γ nuclides in boxed waste. Ato. Ener. Sci. Tech. **58**, 913-921 (2024). **in Chinese**

[38] M. Jandel, M. Morhac, J. Kliman, et al., Decomposition of continuum γ-ray spectra using synthesized response matrix. Nuc. Inst. Meth. Phys. Res. A. **516**, 172-183 (2004). doi: 10.1016/j.nima.2003.07.047